Influence of negative momentum compaction factors on longitudinal beam dynamics in an electron synchrotron

P. Schreiber, * T. Boltz, M. Brosi, B. Haerer, A. Mochihashi, A. I. Papash, M. Schuh, and A.-S. Müller
Karlsruhe Institute of Technology, Karlsruhe, Germany

(Received 19 December 2025; accepted 9 March 2026; published 16 April 2026)

For the development of new synchrotron light sources, new operation modes are considered. For a successful application of these schemes, however, an understanding of the effects involved is essential. The KIT storage ring, Karlsruhe Research Accelerator (KARA), allows the implementation of new operating modes, including tests using a variety of high-performance beam diagnostics devices. Negative momentum compaction optics has been established at KARA at various beam energies. Systematic studies of the resulting beam dynamics showed significant differences to the dynamics at equivalent positive momentum compaction factors. Moreover, a longitudinal instability occurs at low absolute values of the momentum compaction factor, caused by coherent synchrotron radiation, which is the dominant longitudinal impedance at KARA. This work outlines the status of the operation with negative momentum compaction factors at KARA and presents the current-dependent bunch length at negative momentum compaction. Furthermore, the observation of the instability and its dynamics, including significant deviations from threshold predictions, is shown and compared to the equivalent instability at positive momentum compaction.

DOI: 10.1103/wrzc-7d6y

I. INTRODUCTION

Strict requirements for synchrotron light push light sources toward lower emittances and higher intensities. A possible method to fulfill these requirements is the use of multibend achromatic lattices. However, in order to control the chromaticity in these lattices, strong sextupole magnets are necessary, which pose the problem of reduced dynamic aperture. One solution to this problem could be the use of negative momentum compaction factors α_c. This would allow operation with negative chromaticity values and therefore weaker sextupoles, resulting in increased dynamic aperture. These potential improvements for operation set the negative momentum compaction regime up as an active field of research and make the investigation of beam dynamics in this regime particularly interesting.

The electron storage ring KARA [1] of the KIT synchrotron light source is operated as an accelerator test facility. The combination of a flexible lattice with the availability of a variety of fast beam diagnostic systems makes KARA an ideal machine for tests of negative momentum compaction operation [2,3].

The use of negative momentum compaction factors for different use cases in electron machines has been studied before [4–9]. Differences in the beam dynamics for positive vs negative momentum compaction factors are expected. The momentum compaction factor defines the relative path length difference for a relative momentum offset and is a crucial parameter in the longitudinal beam dynamics. Therefore, especially the longitudinal beam dynamics are expected to differ for the two signs of α_c. For example, when changing the sign of α_c, the rotation direction of the charge distribution in the longitudinal phase space is reversed. Wakefields, however, only depend on the bunch profile and the relevant impedance but not directly on the sign of α_c. They represent the interaction of a bunch with itself and its surroundings and can greatly influence the longitudinal charge distribution. Combined with the reversed rotation of the phase space, differences in the longitudinal beam dynamics are expected, including, for example, the current-dependent bunch length or the microbunching instability, which, for short bunches, is quite prominent at KARA and is already extensively studied at positive α_c [10–14]. This instability arises for short bunches, where coherent synchrotron radiation (CSR) is emitted and microstructures appear on the longitudinal charge distribution due to the wakefields caused by CSR [15]. Past studies reported on the bunch length behavior,

*Contact author: patrick.scheiber@kit.edu

e.g., Ref. [4], as well as the energy spread increase, e.g., Ref. [5], due to the microwave instability (mostly caused by resistive wall and geometric impedances). In contrast, the presented studies at KARA are dominated by the CSR impedance due to the short bunches at low absolute values of the momentum compaction factor, giving rise to the microbunching instability.

This paper first introduces the lattice and different optics available at KARA in Sec. II and reports shortly on the current status of the implementation of operation with a negative momentum compaction factor in Sec. III. Section IV describes the longitudinal observations and measurement methods. The second half of this paper focuses on anticipated differences in beam dynamics between the two signs of α_c and highlights observations of additional differences. The effect of negative α_c on the current-dependent bunch length is shown in Sec. V, followed by the effect of the sign of α_c on the observed instability. A conclusion is given in Secs. VII and VIII summarizes and closes this paper.

II. LATTICE AND OPTICS

KARA has a circumference of 110.4 m and a fourfold symmetry consisting of two double bend achromat like structures per cell. Each such structure contains five quadrupoles, where corresponding ones in the different structures are connected to the same power supply as a so-called family. The magnetic structure of a cell is shown at the bottom of Fig. 1. Straight sections between magnetic structures are filled with insertion devices, rf cavities, and injection magnets. The basic parameters of the KARA storage ring are listed in Table I.

TABLE I. Basic parameters of KARA.

Quantity	Value	Unit
Circumference	110.4	m
Energy	0.5–2.5	GeV
Radio frequency f_{rf}	500	MHz
Harmonic number	184	
Nominal momentum compaction factor α_c	9×10^{-3}	
Typical low momentum compaction factor α_c	1×10^{-4}	
Negative momentum compaction factors α_c	-8×10^{-3} – -3×10^{-4}	
Nominal chromaticity Q_x/Q_y	$+1/+1$	
Natural e-spread σ_δ at 0.5 GeV	1.8×10^{-4}	
Natural e-spread σ_δ at 1.3 GeV	4.7×10^{-4}	
Natural e-spread σ_δ at 2.5 GeV	9×10^{-4}	
Bending radius R	5.559	m
Longitudinal damping time τ_d	10.4	ms
Vacuum gap $2h$	32	mm

The momentum compaction factor α_c can be expressed as

$$\alpha_c = \frac{\frac{\Delta L}{L}}{\frac{\Delta p}{p}} = \frac{1}{L} \oint \frac{D(s)}{R(s)} \mathrm{d}s, \tag{1}$$

where L is the path length for one revolution of a particle with design momentum p, and ΔL and Δp denote the deviations of particles with different momenta. D describes the dispersion function and $R(s)$ the local bending radius along the ring at the longitudinal coordinate s. According to this equation, the momentum compaction factor can be modified by changes to the dispersion in sections where the bending radius is finite. For KARA and its lattice, one way

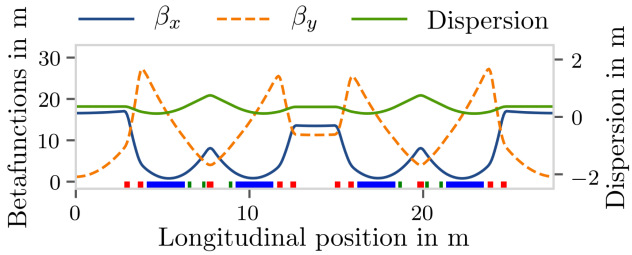

FIG. 1. Calculated betatron functions and horizontal dispersion for standard operation at $\alpha_c = 9 \times 10^{-3}$. The bottom depicts the magnets: quadrupoles in red, sextupoles in green, and bends in blue.

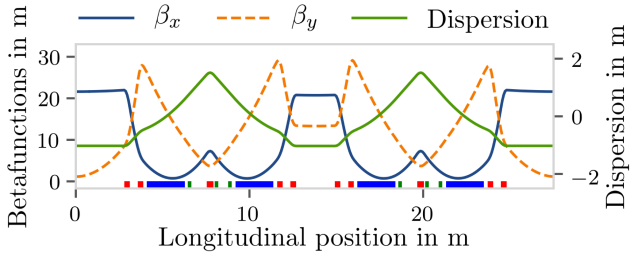

FIG. 2. Calculated betatron functions and horizontal dispersion for short bunch operation at $\alpha_c = 1 \times 10^{-4}$. The dispersion is negative in parts of the bending magnets.

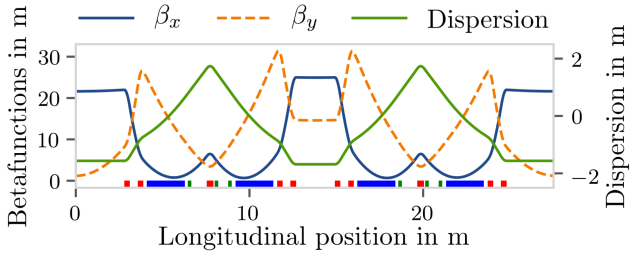

FIG. 3. Calculated betatron functions and horizontal dispersion for operation with a negative momentum compaction factor of $\alpha_c = -8 \times 10^{-3}$. Here the dispersion is largely negative in areas with bending magnets.

to reach smaller values of α_c is to push the dispersion down to negative values by increasing the strength of the field lens quadrupole in the center of the double bend achromat.

At KARA, mainly two established operational optics with different momentum compaction factors exist. At a maximum energy of 2.5 GeV, the standard operational optics with a momentum compaction factor of $\alpha_c \approx 9 \times 10^{-3}$ is used. The optical functions are displayed in Fig. 1. Here the dispersion is positive in the entire section and therefore in the ring, resulting in a positive momentum compaction factor.

At 1.3 GeV, a dedicated short bunch mode exists at various momentum compaction factors, with a minimum at about $\alpha_c \approx 1 \times 10^{-4}$ [16]. Figure 2 shows the optical functions for this operating mode. Note that the dispersion is negative in some areas of the section, resulting in a reduced but still positive momentum compaction factor.

A new mode with various selectable *negative* momentum compaction factors has been implemented. In this case, as shown, for example, in Fig. 3 for $\alpha_c = -8 \times 10^{-3}$, the dispersion is largely negative in parts of the bending magnets resulting in a negative momentum compaction factor.

More information about operational optics at KARA can be found in [17].

III. STATUS OF OPERATION

Operation with negative momentum compaction factors was successfully established at KARA [2] and is now available at various energies [18].

The injection optics for negative α_c was established by starting at injection for positive α_c and stretching the dispersion to reach low values at an injection energy of 500 MeV. Then the quadrupole strengths were extrapolated toward negative momentum compaction factors. The dispersion was stretched by using the field lens quadrupole.

Switching the sign of α_c with a stored beam is not feasible. Therefore, the beam was dumped, and in parallel with the quadrupole magnets, the phase between the injection booster and the storage ring was switched by about π in order to maintain phase focusing. Then injection was resumed and the optics were optimized. More on the implementation technique can be found in [2].

Injection has been achieved for multiple values of α_c with a limit of about 1 mA in single-bunch and about 22 mA in multibunch operation with approximately 120 bunches [2]. During injection, high orbit deviations of up to 8 mm are necessary, which pose the problem of higher order magnetic fields and resulting optics changes caused by beam orbit variations. For the injection into negative α_c optics, reduced sextupole strengths were found to be beneficial [19].

While the injection energy is fixed by the booster energy at 0.5 GeV, the storage ring in general is capable of ramping the energy up to 2.5 GeV, which is routinely used for standard day-to-day operation. At negative α_c, energy ramping has been successfully established to various energies up to 1.3 GeV.[1] At 0.9 GeV, an orbit correction scheme is applied without beam loss, obtaining orbit amplitudes below 0.5 mm while correcting the working point in parallel. This is necessary since the tunes change while reducing the orbit deviations. The reason for this is additional magnetic field components of quadrupoles and sextupoles that are experienced by the beam at high orbit deviations. Afterward, the energy can be freely ramped to higher energies of up to 1.3 GeV. The beam lifetime increases with higher energies as expected due to, e.g., increased radiation damping and reduced Touschek losses [20].

It is also possible to alter the momentum compaction factor with stored beam at the various available energies with an achieved minimum of $|\alpha_c| \approx 3.5 \times 10^{-4}$ at 1.3 GeV. Multiple measurements are being performed using this new optics at negative α_c, including the ones shown in the following sections.

IV. LONGITUDINAL OBSERVATION TECHNIQUES

With a working negative α_c mode at KARA, it is possible to observe and investigate the beam dynamics of this new mode in order to evaluate it for future use. As described in the introduction, α_c is a longitudinal parameter and therefore has a significant influence on the longitudinal beam dynamics. It changes the movement of particles in the longitudinal phase space, and, for example, a change in sign necessitates a shift in acceleration rf phase by around 180°, which, together with the changed sign of α_c, reverses the natural rotation in the longitudinal phase space. However, some effects such as the generation of radiation or wakefields are not directly affected by the sign of α_c and act back unaltered on the longitudinal phase space, which changes the dynamic behavior of a bunch even further. For these reasons, investigations on the longitudinal dynamics of the negative α_c regime at KARA were performed by observing the current-dependent bunch length and the dynamics of emitted CSR in the THz frequency range due to longitudinal instabilities. These observations were conducted at an energy of 1.3 GeV. This section introduces the measurement methods used to observe the change in dynamics.

A. Bunch length measurement method

The bunch length at KARA can be measured with a dual sweeping streak camera.[2] The fast time axis is used to resolve the bunch length with the streak time set to the smallest value of 190 ps. The slow time axis is used to resolve the evolution of the bunch length over time. Its value is set in such a way that multiple synchrotron oscillations can be observed while an adequate intensity

[1]Energies up to 2.5 GeV are theoretically possible but were not the focus of this study.

[2]Model: Hamamatsu C5680.

of the streak image is still kept and varies depending on the machine settings used.

During the natural decrease of bunch current, a measurement sequence consisting of 100 images with a duration of around 8 s per sequence was taken every 10 s. After correcting for center-of-mass movements, due, for example, to synchrotron motion, the longitudinal profiles resulting from the images are averaged and a full width half maximum bunch length is calculated.

In [21], the accuracy of the described measurements was determined to be better than $\Delta l < 0.3$ ps.

B. THz measurement method

The IR beamlines at KARA allow the observation of CSR in the THz frequency range. Using fast THz sensitive Schottky barrier diode detectors [22] combined with the fast readout system KAPTURE [23], it is possible to record the THz radiation intensity bunch-resolved turn-by-turn. The temporal development of the measured THz intensity serves as an indication of the dynamics of the longitudinal bunch profile. Measurements shown in Sec. VI were taken with a broadband zero bias diode from ACST [22] with an approximate sensitivity range of 50 GHz to 1 THz. This setup is routinely used for studies at positive α_c [12], where the acquisition system is synchronized to the revolution clock of KARA. For the measurements presented in this paper, the setup was used for the first time at negative α_c settings. This was possible due to the quite flexible timing capabilities of KAPTURE, where the sampling time can be shifted by half an rf period to match the phase of the bunch at negative α_c.

To resolve the temporal properties of the dynamics in the THz radiation and to reduce the amount of generated data, the THz power of only every 10th turn was recorded for each bunch over a duration of 1 s, resulting in a frequency resolution of 1 Hz. To observe the current dependent dynamics of the beam, measurements over a wide range of currents are necessary.

During such measurements, the current decrease of one bunch is typically observed for a few hours. Due to the time they require, those measurements would limit the number of values of α_c to observe. Therefore, a different measurement method, called the snapshot method [13] and originally implemented at low positive α_c settings, was applied for some measurements. This method can circumvent the time requirements by sacrificing current resolution for speed. It exploits a special filling pattern, where the desired current range is spread over different bunches. This is possible, as it was shown for positive α_c that multibunch effects are below the detection accuracy if at all present [24]. The validity for negative α_c was confirmed at random sample points for both voltages shown here. To regain some current resolution, this method was developed further into so-called snapdecays. These combine the traditional measurement technique of letting the current naturally decrease with the snapshot technique using a special filling pattern by merging multiple snapshot measurements into one. Such a measurement takes in the order of a few minutes. Bunches of the different snapshot measurements are treated equally and sorted by their respective, momentary current, resulting in a higher effective current resolution. As the lifetime in negative α_c mode at KARA is rather low (≈30 min at negative α_c and 0.1 mA bunch current vs ≈90 min at positive α_c and also 0.1 mA bunch current), the necessary current range to fill the gaps in the available bunch currents from the filling pattern is quickly traversed.

C. Bunch current measurement method

As the snapshot and snapdecay measurement methods employ multibunch filling patterns, a detailed knowledge of the individual bunch currents is crucial. In order to assign a current for each bunch at each measurement, a time correlated single photon counting setup is used [25]. Due to construction work at KARA, this setup was temporarily located at an IR beamline instead of the visible light diagnostics port, resulting in lower count rates and therefore slightly higher statistical errors. The photon counting follows a Poisson distribution, hence with a typical count rate of 3000 counts this results in a relative current error of $\delta = \frac{1}{\sqrt{3000}} = 0.018 = 1.8\%$. For a bunch current of 0.08 mA, this would result in an absolute error of $\Delta = \pm 1.46$ μA. When sorting the signals of multiple bunches for a snapdecay measurement, these errors could result in uncertainties in the sorting order of the signals and will be considered in the evaluation of the results.

D. Simulations

Accompanying simulations to the measurements were performed using Inovesa [26]. Inovesa is a longitudinal Vlasov-Fokker-Planck solver, routinely used at KARA to study the longitudinal beam dynamics [11,14,24,27,28]. While Inovesa can work with arbitrary impedances, the most prominent, due to the short bunches at KARA, is the parallel plates impedance. Inovesa simulations using this impedance have been shown to fit well to the measurements at positive α_c [27]. For the comparison shown in this paper, Inovesa was extended to allow for simulations in the negative momentum compaction regime. Since Inovesa simulates a given time range for a fixed bunch current, the current dependence of effects was simulated by performing multiple simulation runs with different bunch currents distributed evenly over the desired current range. In general, these simulations were performed for the same machine settings used in the shown measurements.

V. CURRENT-DEPENDENT BUNCH LENGTH

The equilibrium bunch length in an electron storage ring is influenced by phase focusing, which in turn depends on the gradient of the electric potential experienced by the

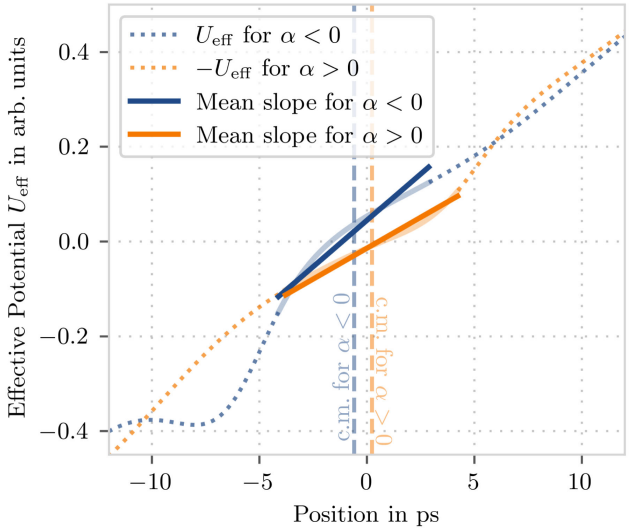

FIG. 4. Effective potential U_{eff} of an example case for positive and negative α_c. The potential for positive α_c was flipped in the display to simplify comparison. Here the dotted lines represent the effective potential while the solid, light lines represent the potential in an area where the bunch is located. The solid, intense lines show the mean gradient over the bunch as an aid. Two dashed, vertical lines indicate the location of the center of mass for both signs of α_c. The wake potential used here was calculated using Inovesa [26] using the CSR parallel plates impedance.

individual particles. The simplest approach would only consider the rf potential. This would then result in no bunch length changes with current, as the potential is constant. However, this changes when taking the longitudinal wakefields, generated by the interaction of the bunch with its environment, into account. Thus, the effective potential U_{eff} as the sum of rf potential and wakefields[3] is considered

$$U_{\mathrm{eff}}(I) = U_{\mathrm{rf}} + U_{\mathrm{Wake}}(I). \tag{2}$$

As the wakefield of a bunch is dependent on the bunch charge so is the effective potential, which means the bunch length is changing with bunch current I.

In order to maintain phase focusing, operation with negative α_c requires an rf phase shifted by about π, which means the rf potential is reversed with respect to the one seen by a bunch in a machine with positive α_c. This results in a different gradient of the effective potential [Eq. (2)] and therefore in a different bunch length [18].

Considering the CSR parallel plates impedance [30] for short bunches, the dominant impedance at KARA (due to small absolute values of α_c), the average gradient of the effective potential U_{eff} is larger for negative than for positive α_c at low currents. In fact, for negative α_c the gradient of U_{eff} is larger than for the unperturbed pure rf potential, while it is smaller in the case of positive α_c. An example is shown in Fig. 4.

This means that, since with increasing current the wake potential increases, the mean gradient of the effective potential increases for negative α_c and decreases for positive α_c. Consequently, the bunch length increases with current for positive α_c and decreases for negative α_c.

It is therefore expected to observe a different current dependent behavior of the bunch length for different signs of α_c.

A. Simulations

At KARA, the usual negative α_c operating mode uses low absolute values of α_c (in the order of 1×10^{-4}). Therefore, only the case of short electron bunches is considered in the following section. The most prominent longitudinal impedance in this case is the parallel plates CSR impedance.

Using Inovesa [26], the longitudinal phase space was simulated with the same absolute value $|\alpha_c| \approx 4 \times 10^{-4}$, once for a positive and once for a negative sign of α_c. The resulting bunch length as function of bunch current is shown in Fig. 5. Similar results for bunch shortening were found in [31], where they considered wakefields resulting from geometric and resistive wall effects.

Inovesa simulates a given time range for a fixed bunch current, therefore, one simulation run was performed for each bunch current. The bunch length is calculated as full width half maximum from the resulting bunch profiles and averaged over time for each simulated bunch current. The fluctuation range is calculated above and below the mean individually by calculating the standard deviation with

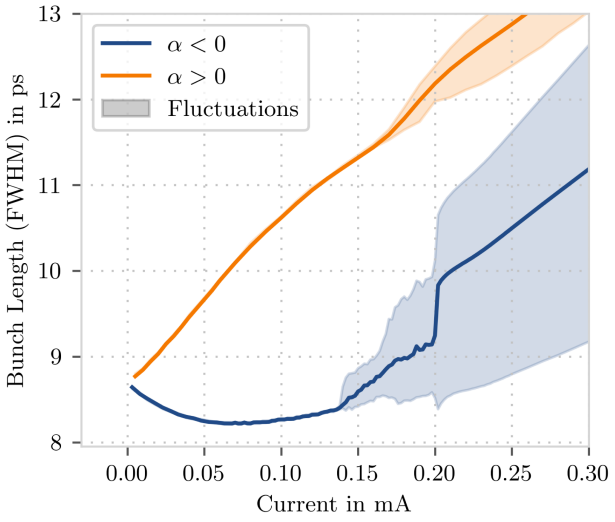

FIG. 5. Bunch length simulated with Inovesa for both signs of α_c with the same absolute value. Solid lines denote the mean bunch length over time while the shaded area denotes the fluctuation region over time per bunch current.

[3]A similar concept was used to study the synchrotron motion during the microbunching instability in [29].

respect to the overall mean for just the data points above or below the mean, respectively.

Clearly, for positive α_c, the bunch length increases with current. As the wake potential effectively lowers the gradient of the effective potential in this case, this behavior is expected. However, for negative α_c at low currents, the bunch length shows bunch shortening. For those low bunch currents the bunch profile is almost of Gaussian shape and almost identical for positive and negative α_c, apart from the different bunch length. Therefore, also the wake potential is similar. Due to the reversed rf voltage necessary at negative α_c, the gradient of the effective potential is increased in this case. This results in lower bunch lengths. For low bunch currents, in the shown simulation roughly up to 0.06 mA, where the bunch profile is only slightly distorted compared to a Gaussian shaped profile, the wake potential roughly scales with bunch current. Therefore, the bunch length reduces with current as seen from the simulation in Fig. 5.

At higher currents, the bunch is deformed due to the self-interaction with its own wakefield. This perturbs the previous behavior by changing the shape of the wakefield and leads to an increase in bunch length. While at low currents no fluctuations in bunch length are visible this is not the case at higher currents. Such fluctuations were already seen in [32] and in conjunction with coherent synchrotron radiation emission bursts in [33]. For positive α_c these fluctuations start at roughly 0.160 mA and for negative α_c at about 0.137 mA for the simulated parameters. These fluctuations are caused by the microbunching instability, which leads to nonstatic deformations of the bunch profile [33]. For negative α_c at about 0.20 mA, a sharp increase in bunch length is visible. This is due to a change of the behavior of the instability, which manifests in even larger deformations of the bunch profile and corresponding bunch length.

B. Measurements

Bunch length measurements were conducted for the same absolute value of α_c as used in the simulations for both signs. All measurements were performed during single-bunch operation to exclude effects of bunch interaction or overlapping images on the streak camera. The results are shown in Fig. 6.

Solid lines in Fig. 6 refer to a moving average of the data while shaded areas display the statistical fluctuations calculated as standard deviation from up to 10 measurement points at similar bunch currents, assuming the bunch length changes slowly compared to the acquisition speed.

The measurements for positive α_c show a bunch lengthening comparable to the simulations and the measurements for negative α_c show bunch shortening. Measurements at UVSOR [5] and at the Diamond Light Source [8] gave similar results.

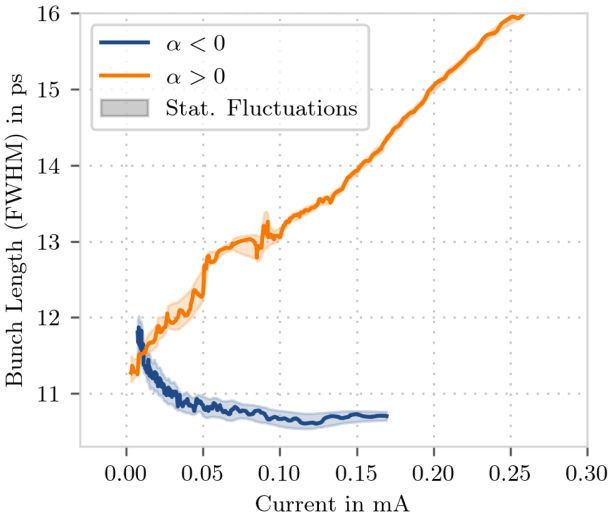

FIG. 6. Bunch length measured using a streak camera for positive α_c and negative α_c with the same absolute value of α_c. Solid lines represent a moving average and the shaded areas represent the statistical fluctuations calculated from multiple measurements for similar currents.

Since the slow time axis of the streak camera is chosen to resolve the synchrotron oscillation it cannot resolve single turns. Therefore, the bunch length fluctuations seen in simulations are not visible in these measurements. However, parallel measurements with KAPTURE and a Schottky diode (cf. Sec. IV B) show that the microbunching instability occurred above approximately 0.150 mA for positive α_c. For negative α_c, a threshold of the instability at about 0.08 mA was observed. Due to operational limitations, the bunch currents for negative α_c were limited to 0.17 mA during these measurements.

C. Comparison

Similar to the simulations, the positive α_c bunch length increases with current in measurements. In the area between 0.05 and 0.1 mA, an unexpectedly increased bunch length was measured. The reason for this is still under investigation. Apart from that and a general offset of about 2 ps in the FWHM bunch length, the measurement fit quite well to the simulations.

The measured bunch length for negative α_c displays a bunch shortening for low bunch currents similar to the shortening seen in simulations. For almost zero current, the bunch length for negative α_c seems to be higher than for positive α_c, which is not expected from both simulations and theoretical considerations. This effect hints at an offset between the bunch length measurements for the two signs of α_c caused by the experimental conditions.

The otherwise good agreement for the evolution of bunch length over current also indicates a good fit of the used impedance for the simulations.

Further studies should focus on increasing the bunch current for these measurements in order to study the effect of the instability on the bunch length observed in simulations.

VI. OBSERVED INSTABILITY

At positive α_c as well as negative α_c, an instability has been observed above a certain threshold current, which can be seen in the intensity fluctuations of the coherent THz radiation generated by the beam. For positive α_c, the instability was identified as the microbunching instability by synchronous measurements of the energy spread, longitudinal bunch profile, and THz intensity [11], which is explained in the next section. The reason why the same mechanism could be different for negative α_c is explained as well. Following sections will present the results of measurements and simulations for negative α_c, including comparisons to positive α_c results.

A. Microbunching instability

Reducing the absolute value of the momentum compaction factor leads to shorter bunches. This increases the spectral range of emitted coherent synchrotron radiation (CSR) up to higher frequencies. The emitted CSR power scales with the number of emitting particles squared. This intense radiation can enable significant interaction between the bunch and its emitted radiation, leading to structures in the longitudinal phase space density and subsequently leading to substructures on the longitudinal bunch profile. Since these structures are short by nature, they lead to CSR emission at higher frequencies and therefore result in further self-interaction of the bunch with its radiation. At the same time, these substructures lead to a lengthening of the bunch and subsequently smear out. Together with radiation damping, the now longer bunch profile leads to a bunch shortening, and thus the CSR interaction increases again, resulting in growing substructures. After reaching a critical bunch length, a cycle evolves and the process starts anew by lengthening the bunch again. It is important to note that this instability does not necessarily lead to immediate beam loss. A more detailed description of the microbunching instability is given in [12].

This instability has been thoroughly studied for the positive momentum compaction regime, e.g., in [24]. The interaction between the bunch and its radiation can be described by longitudinal wakefields produced by the radiation. These wakefields are longitudinally not symmetric around the center of the bunch.

As previously described, the phase space density of a bunch in a synchrotron light source rotates with a direction that depends on the sign of α_c. Together with the asymmetric wakefields, a different behavior caused by the CSR self-interaction is expected for a change in sign of α_c.

B. Spectrograms

A useful and widely used technique to visualize the beam dynamics during a longitudinal instability leading to CSR emission is the use of CSR intensity fluctuation spectrograms. Some examples are shown in Fig. 7. Employing the acquisition techniques described in Sec. IV B, a set of THz measurements consisting of multiple datasets corresponding to different currents was acquired for each setting, such as α_c and acceleration voltage. By calculating the fast Fourier transform and sorting by bunch current, the current dependent frequency content of the fluctuations in the THz intensity can be visualized in so-called spectrograms, as seen in Fig. 7. Each line corresponds to one measurement[4] and the width of each line is determined by the bunch current at the time of measurement (lower edge) and the next higher current for which a measurement exists (upper edge). This technique has been used for analysis of the microbunching instability at positive α_c [13]. A typical spectrogram measured at positive α_c is shown in Fig. 7(a). Certain characteristic features of the instability are visible. An important feature is the threshold of the instability, which is the bunch current below which close to no fluctuations are observed [e.g., 0.115 mA in Fig. 7(a)]. Further visible features include the frequency of the fluctuations at the threshold [e.g., 25.4 kHz in Fig. 7(a)] and the current dependent behavior of the dominant fluctuation frequencies.

In Fig. 7(b), a spectrogram for a measurement at equivalent settings with a negative sign of α_c is shown. The spectrograms differ drastically. While both show a threshold of the instability, for positive α_c the structure starting from the threshold upward changes greatly over current and the equivalent structure for negative α_c just broadens a little with higher currents. It is important here to note that, due to technical difficulties, the measurements for negative α_c are limited in current range and do not reach as high currents as the measurements for positive α_c. Measurements at the Diamond Light Source [34] show a similar change from complex structures to more or less vertical lines when switching from positive to negative momentum compaction factors. This strong difference in the measurements at positive and negative momentum compaction factors hints at a different behavior in the longitudinal phase space.

The behavior at positive α_c seen in Fig. 7(a) is caused by the microbunching instability and can be completely described by longitudinal beam dynamics [12]. The negative α_c measurements in Fig. 7(b) are drastically different from the positive α_c ones. Based on these measurements alone, it is not clear if the differences are caused by additional effects that are not considered in the longitudinal dynamics of the microbunching instability. However, purely longitudinal simulations with Inovesa shown in

[4]THz intensity signal measured over 1 s for a single bunch.

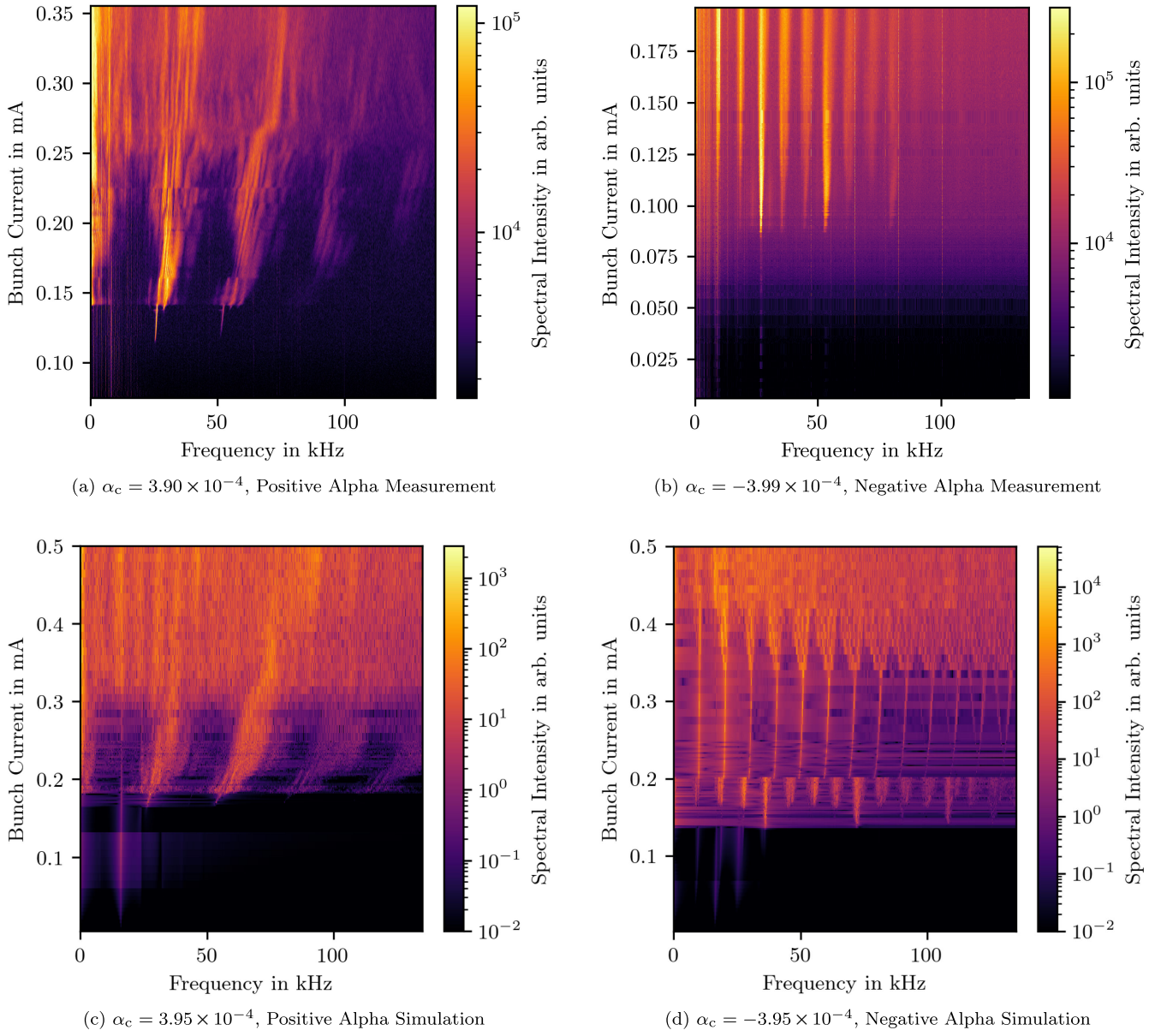

(a) $\alpha_c = 3.90 \times 10^{-4}$, Positive Alpha Measurement

(b) $\alpha_c = -3.99 \times 10^{-4}$, Negative Alpha Measurement

(c) $\alpha_c = 3.95 \times 10^{-4}$, Positive Alpha Simulation

(d) $\alpha_c = -3.95 \times 10^{-4}$, Negative Alpha Simulation

FIG. 7. THz intensity fluctuation spectrograms for an accelerating voltage of 1000 kV. (a) Shows a measurement for positive α_c measured using the traditional measurement method, following the current decrease of a single bunch. (b) Shows an equivalent measurement for negative α_c, for which the data were taken using the snapdecay method. (c) Shows an equivalent simulation for positive α_c. (d) Shows an equivalent simulation for negative α_c. Note the observed bunch current range of these spectrograms differs for the different figures.

Figs. 7(c) and 7(d) for both signs of α_c agree and differ from each other in similar ways than the measurements. This strongly indicates a mostly longitudinal cause of the dynamics seen at negative α_c. Additionally, the simulations at higher bunch currents reveal more complex dynamics also in the negative α_c case.

Figure 8 shows a close-up of a spectrogram on the most prominent feature, just above the instability threshold. This spectrogram was measured at settings with a slightly relaxed bunch length, where at about 0.153 mA a change in the width of the dominant structure occurs. This could hint at more complex behavior occurring at higher currents and could be related to the change visible in the simulation in Fig. 7(d) at about 0.2 mA. Note, the measurements shown in Fig. 8 were not taken with uniformly distributed bunch currents, leading to single higher "pixels," e.g., at 0.13 mA, where the measurement below was stretched up. These lines seem to contain more narrow structures than the surrounding lines, however, as it is only a single measurement no effects can be established from that.

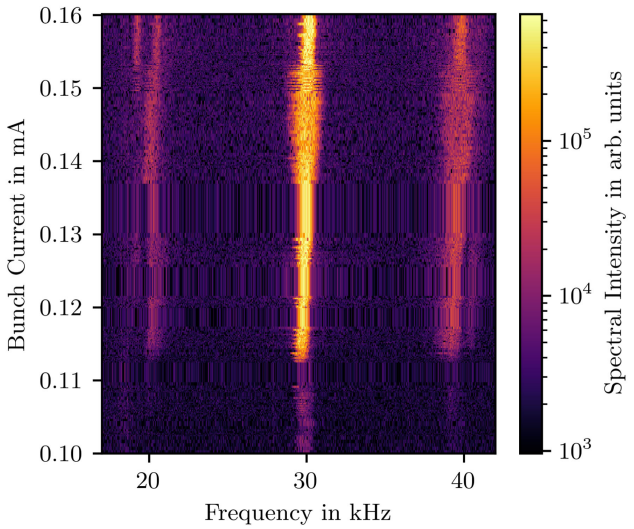

FIG. 8. THz fluctuation spectrogram for negative momentum compaction factor of $\alpha_c = -5.0 \times 10^{-4}$ and an acceleration voltage of 1000 kV. At higher currents at about 0.153 mA the structures get slimmer hinting at more complex dynamics and behavior over current.

The generation of the CSR intensity is rooted in the bunch profile as well as the CSR impedance. Therefore, the longitudinal bunch profile can be used as indication of the dynamics as well. Figure 9 shows different bunch profiles below and above the respective threshold for positive and negative α_c simulations corresponding to the simulations shown in Figs. 7(c) and 7(d). Below the threshold, the effect of the bunch shortening is visible together with the effect of higher charge density toward the tail of the bunch (negative position in the plot) at negative α_c and toward the head of the bunch at positive α_c. This results in the expected leaning in opposite directions following the Haissinski distribution. At higher currents, significantly above the instability threshold, the dynamic substructures are visible and show stronger deformations in the negative α_c case. At 200% of the instability threshold current I_{th}, the negative α_c case shows a smooth continuous transition between two states corresponding to the regular pattern seen in the spectrogram in Fig. 7(d). In the positive α_c bunch profiles at 200% threshold current, a high number of smaller, narrower structures is visible, corresponding to a high number of structures in the longitudinal phase space, compared to the negative α_c case. Due to the rotation in phase space, this higher number of structures leads to constructive overlapping at certain repetition frequencies and partial overlapping at intermediate frequencies, corresponding to the "washed out" structures seen in the spectrogram in Fig. 7(c).

From the shown measurements and simulations, including the bunch profiles, it is visible that the threshold of the instability is significantly lower for negative α_c which will be discussed in the following section.

C. Instability threshold

The instability threshold is the lowest bunch current above which the instability occurs.

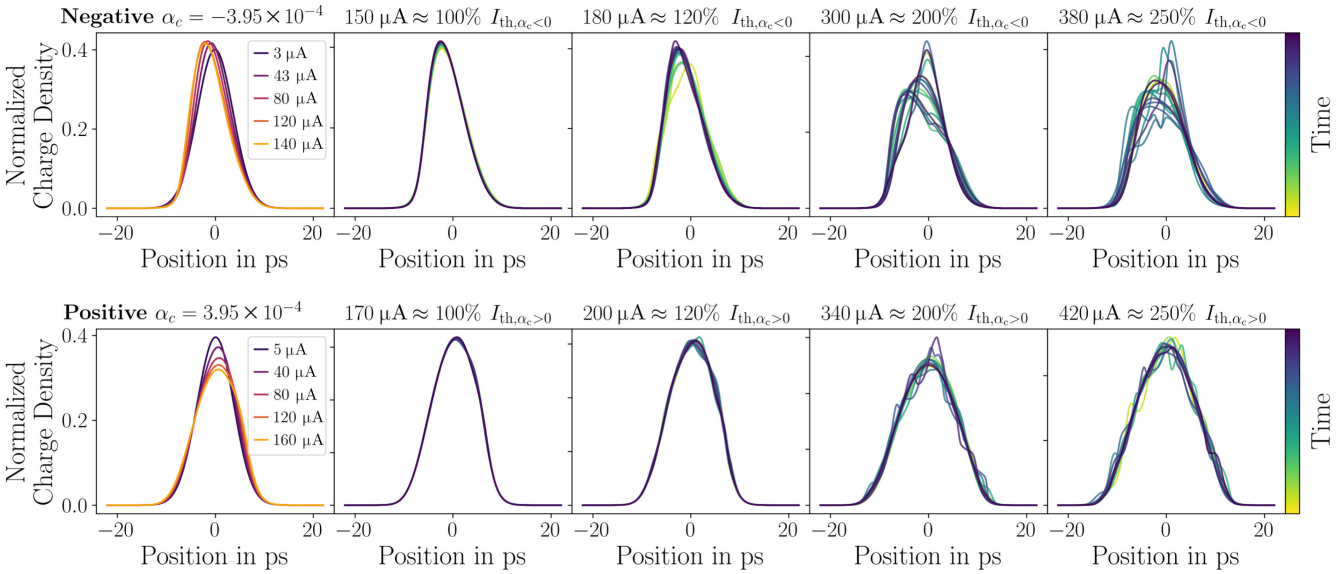

FIG. 9. Bunch profiles from simulations at negative α_c (top) and positive α_c (bottom) with $|\alpha_c| = 3.95 \times 10^{-4}$. The left most panel shows bunch profiles at different bunch currents below the instability threshold and the remaining four panels show the profiles for various bunch currents at and above the threshold. In the stable case, the colors represent different bunch currents and the evolution from almost Gaussian shape toward a Haissinski shape is visible, while in the unstable case, the colors indicate different points in time during the instability representing the dynamic evolution of the bunch profile and their substructures over time.

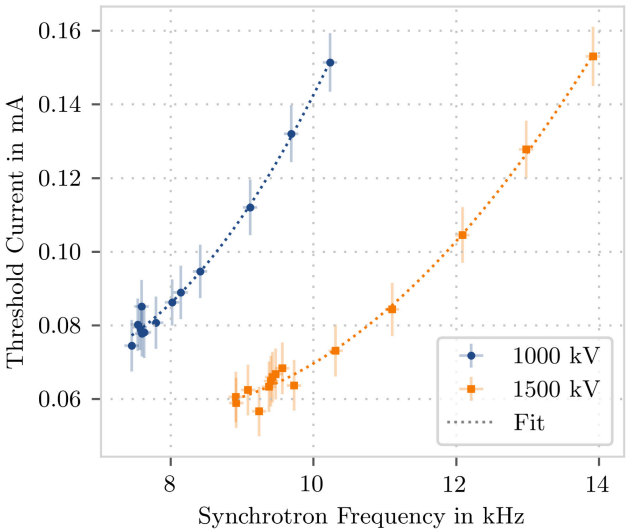

FIG. 10. Threshold current as a function of synchrotron frequency for an acceleration voltage of 1000 and 1500 kV. Clearly visible is the higher threshold for the lower voltage as the bunch is longer compared to the higher voltage case. Dashed lines show a second order polynomial fit. The fit results for the fit function $I_{\mathrm{th}}(fs) = a + b \times fs + c \times fs^2$ are $a_1 = 0.254(\pm 0.103) b_1 = 0.060(\pm 0.024) c_1 = 0.0049(\pm 0.0013) a_2 = 0.205(\pm 0.042) b_2 = 0.039(\pm 0.009) c_2 = 0.0025(\pm 0.0003)$, where the index 1 indicates values for 1000 kV and the index 2 for 1500 kV.

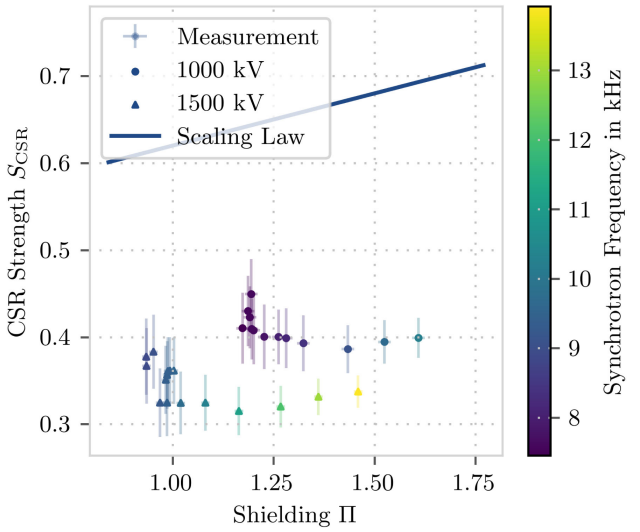

FIG. 11. Instability thresholds at negative α_c in units of S_{CSR} as a function of Π. The solid line marks the scaling law for positive α_c as reference. The color of measurement points indicates the synchrotron frequency for each measurement and the shape of the points indicates the voltage for each measurement. Errors shown here are the result of error propagation from the values shown in Fig. 10.

For several measurements at different values of α_c and accelerating voltage the instability threshold was determined, since both parameters influence the natural bunch length. Figure 10 shows the threshold currents for two accelerating voltages as a function of synchrotron frequency. Here the synchrotron frequency serves as measurable indication of the momentum compaction factor.[5]

The uncertainty on the synchrotron frequency was determined as 100 Hz effective resolution and signal-to-noise ratio of the bunch-by-bunch system [35,36]. The current error on the threshold currents was determined as maximum error of 7–9 μA consisting of 5 μA reading error from the determination of the threshold from the spectrograms and the Poisson error of the current measurement.

Measurements for both voltages shown in Fig. 10 seem to follow a second order polynomial and the dotted line in Fig. 10 depicts a second order polynomial fit. The two cases differ in the coefficients of the polynomial. However, as expected, both cases increase in threshold current with increasing bunch length indicated by the synchrotron frequency (for a fixed voltage). Also, the thresholds for 1500 kV are lower compared to those for 1000 kV, which is expected since the bunch length is shorter in that case as well, resulting in a higher charge density and additionally in emission of CSR up to higher THz frequencies.

As previously seen, corresponding measurements at positive α_c of the microbunching instability [24,37,38] show a clear threshold as well. In that regime, a prediction for the instability threshold was derived from simulations at positive α_c in [39]. This prediction will be called "scaling law" in this paper. Often the dimensionless parameters Shielding Π and CSR strength S_{CSR} are used, where the threshold of the instability takes a linear form [39]

$$S_{\mathrm{CSR}}|_{\mathrm{th}} = 0.5 + 0.12\Pi \tag{3}$$

with

$$\Pi = \frac{\sigma_{z,0} R^{1/2}}{h^{3/2}}, \tag{4}$$

$$S_{\mathrm{CSR}} = \frac{r_e N_b}{2\pi \nu_s \gamma \sigma_{\delta,0}} \frac{R^{1/3}}{\sigma_{z,0}^{4/3}} = \frac{c I_b R^{1/3}}{2\pi \gamma f_s \sigma_{\delta,0} I_A \sigma_{z,0}^{4/3}}, \tag{5}$$

where r_e is the classical electron radius, ν_s the synchrotron tune, $\sigma_{z,0}$ is the natural bunch length, R is the bending radius, h is half the height of the vacuum chamber, I_b is the bunch current, γ is the relativistic gamma factor, $\sigma_{\delta,0}$ is the natural energy spread, and I_A is the Alfvén current.[6] The instability thresholds for the negative α_c measurements are shown in Fig. 11 using these dimensionless parameters.

[5]The synchrotron frequency is influenced by the acceleration voltage as well as the momentum compaction factor. For a fixed acceleration voltage, an increase in α_c manifests as an increase in synchrotron frequency.

[6]Alfvén current $I_A = 4\pi\epsilon_0 m_e c^3/e = 17045$ A.

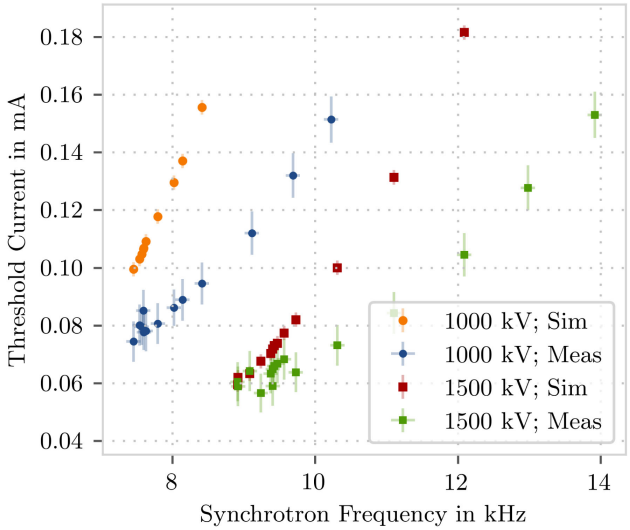

FIG. 12. Instability thresholds as a function of synchrotron frequency for 1000 and 1500 kV. The simulated thresholds show a different slope and differ more from the measurements at higher values of the synchrotron frequency. Note that not for all measurement points a simulation is shown.

For positive α_c it has been shown that measurements correspond quite well to the scaling law [24]. For negative α_c, however, it is easily visible from Fig. 11 that the threshold currents are significantly lower than the scaling law. Previous measurements of the energy spread [5] at UVSOR at negative α_c for longer bunches indicated a lower threshold as well.

Figure 11 shows a nonlinear dependency of the threshold CSR strength on the shielding parameter in the negative α_c case. Furthermore, the thresholds for the two different voltages are not interleaved meaning the voltage has additional significance compared to the scaling law and positive α_c measurements. However, thresholds for both voltages behave similarly and seem to be shifted with regard to each other. Therefore, the behavior of the dynamics at negative α_c is significantly different to positive α_c and most likely no linear scaling law can be found.

Both simulated and measured threshold currents are shown in Fig. 12. For the determination of the thresholds in simulations a region of 100 μA around the corresponding measured thresholds was simulated and the onset of the fluctuation frequencies in the CSR emission determined. The simulated thresholds show a different slope than the measurements. Results in [40] for positive α_c show the simulations systematically above the measurements with the deviations increasing for higher values of the synchrotron frequency. For negative α_c, this effect is even larger. In Fig. 12, the simulations come close to the measurements at low values of the synchrotron frequency and differ more at higher values.

The simulations use a pure parallel plates impedance model which might not completely describe the real machine. Also, the simulations were carried out using a purely linear α_c neglecting all higher orders. As the sextupoles were changed drastically compared to positive α_c the higher orders could differ significantly. Both could be reasons for the mismatch between simulation and measurement and should be verified in the future.

VII. CONCLUSION

Differences in the longitudinal beam dynamics for positive α_c and negative α_c were observed. The measured bunch shortening for negative α_c with increasing bunch current (for currents up to roughly 0.06 mA) fits well to the expected change in beam dynamics due to the necessary change of the acceleration phase by approximately π. Differences are also present between the observed longitudinal instability at negative α_c and at positive α_c and visible by measuring the THz intensity. This instability can be visualized in radiation intensity fluctuation spectrograms. The spectrograms clearly show different characteristics for the microbunching instability at positive α_c and the instability at negative α_c. Simulations considering only longitudinal dynamics show a comparable behavior to the measurements at negative α_c, which hints at a longitudinal origin of the different instability dynamics.

The threshold current of the instability is systematically lower for negative α_c compared to positive α_c. Furthermore, the influence of the synchrotron frequency and the shielding parameter Π is different. The scaling law for the instability threshold, valid for positive α_c, is not applicable here and the behavior differs fundamentally. A reason could be the bunch length, which was shown to be shorter at negative α_c, resulting in higher charge densities that could lead to more CSR emission in relevant frequency ranges and jump start the instability at lower bunch currents.

Furthermore, there are some discrepancies between measurements and simulations, where the simulations show differences in the behavior of the instability threshold as well as an offset in bunch length compared to the measurements. An explanation could be the neglected higher orders of α_c in the simulations. This could, in addition to a difference in threshold, also lead to slightly different dynamics shown in the spectrograms and also cause an offset in bunch length. Considering additional effects, e.g., transversal effects and impedances, could help to improve the simulations further.

Nevertheless, the simulated spectrograms predict comparable differences between positive and negative α_c as were observed in measurements, indicating that the general description of the beam dynamics in the simulations is applicable.

VIII. SUMMARY

At KARA, a negative momentum compaction operating mode has been implemented at multiple energies. Studies in this mode were performed to understand the beam

dynamics in the new regime for future use. The bunch length was measured using a streak camera, THz intensity was measured to investigate the longitudinal instability and simulations were performed corresponding to these measurements. The bunch length at negative α_c was found to be smaller and the threshold of the instability to be lower as well which should be considered when evaluating the use of this mode in future machines. The instability shows similarities to the microbunching instability present at positive α_c; however, some significant differences in its behavior were observed. The performed simulations support the expected longitudinal origin of the observed instability. Simulations considering higher orders of α_c are planned to investigate the discrepancy between simulation and measurement. Furthermore, measurements at higher bunch currents should be performed to further understand the difference in beam dynamics between positive and negative momentum compaction factors α_c. Overall, the presented results provide valuable insights into the involved beam dynamics and support informed decisions toward the use of negative momentum compaction operation for future synchrotron light sources.

ACKNOWLEDGMENTS

This project has received funding from the European Union's Horizon 2020 Research and Innovation programme under Grant Agreement No. 730871. P. S. and T. B. acknowledge the support by the DFG-funded Doctoral School "Karlsruhe School of Elementary and Astroparticle Physics: Science and Technology."

DATA AVAILABILITY

The data that support the findings of this article are not publicly available upon publication because it is not technically feasible and/or the cost of preparing, depositing, and hosting the data would be prohibitive within the terms of this research project. The data are available from the authors upon reasonable request.

[1] E. Huttel, A. B. Kalefa, I. Birkel, A.-S. Müller, P. Wesolowski, F. Perez, M. Pont, and M. Giovannozzi, Operation with a low emittance optics at ANKA, in *Proceedings of the 2005 Particle Accelerator Conference, PAC'05, Knoxville, TN* (JACoW, Geneva, Switzerland, 2005), pp. 2467–2469, https://jacow.org/p05/papers/RPAE037.pdf.

[2] P. Schreiber, T. Boltz, M. Brosi, B. Härer, A. Mochihashi, A.-S. Müller, A. Papash, M. Schuh, H. T. Boland, D. Button, and R. Dowd, Status of operation with negative momentum compaction at KARA, in *Proceedings of the IPAC-2019, Melbourne, Australia*, edited by M. Boland, H. Tanaka, D. Button, and R. Dowd (JACoW, Geneva, Switzerland, 2019), Vol. 10, pp. 878–881, 10.18429/JACoW-IPAC2019-MOPTS017.

[3] P. Schreiber, M. Brosi, B. Härer, A. Mochihashi, A.-S. Müller, A. Papash, R. Ruprecht, and M. Schuh, Beam dynamics observations at negative momentum compaction factors at KARA, in *Proceedings of the IPAC-2022* (JACoW, Geneva, Switzerland, 2022), 10.18429/JACOW-IPAC2022-THPOPT006.

[4] M. Zobov, D. Alesini, M. Biagini, A. Drago, A. Gallo, C. Milardi, P. Raimondi, B. Spataro, and A. Stella, Daϕne experience with negative momentum compaction, in *Proceedings of European Particle Accelerator Conference, EPAC'06, Edinburgh, UK* (JACoW, Geneva, Switzerland, 2006), pp. 989–991, https://proceedings.jacow.org/e06/PAPERS/TUODFI02.pdf.

[5] M. Hosaka, J. Yamazaki, T. Kinoshita, and H. Hama, Longitudinal beam dynamics on an electron storage ring with negative momentum compaction factor, in *Proceedings of the APAC'98, Tsukuba, Japan* (JACoW, Geneva, Switzerland, 1998), pp. 426–428, https://proceedings.jacow.org/a98/APAC98/5D018.PDF.

[6] A. Nadji, P. Brunelle, G. Flynn, M. Level, M. Sommer, and H. Zyngier, Experiments with low and negative momentum compaction factor with super-ACO, in *Proceedings of the EPAC-1996*, WEP090G (1996), https://accelconf.web.cern.ch/Accelconf/e96/PAPERS/WEPG/WEP090G.PDF.

[7] H. Ikeda, J. W. Flanagan, H. Fukuma, S. Hiramatsu, T. Ieiri, H. Koiso, T. Mimashi, and T. Mitsuhashi, Negative momentum compaction at KEKB, arXiv:physics/0401155.

[8] I. P. S. Martin, G. Rehm, C. Thomas, and R. Bartolini, Experience with low-alpha lattices at the Diamond Light Source, Phys. Rev. ST Accel. Beams **14**, 040705 (2011).

[9] P. Kuske, CSR-driven longitudinal single bunch instability with negative momentum compaction factor, in *Proceedings of the IPAC-2016, Busan, Korea* (2016), pp. 1651–1654, 10.18429/jacow-ipac2016-tupor003.

[10] A. S. Müller *et al.*, Experimental aspects of CSR in the ANKA storage ring, ICFA Beam Dyn. Newsl. **57**, 154 (2012), https://e-publishing.cern.ch/index.php/icfa-beam-dyn-newsl/issue/view/216/184.

[11] M. Brosi, T. Boltz, E. Bründermann, S. Funkner, B. Kehrer, A.-S. Müller, M. Nasse, G. Niehues, M. Patil, P. Schreiber, P. Schönfeldt, J. Steinmann, H. T. Boland, D. Button, and R. Dowd, Synchronous measurements of electron bunches under the influence of the microbunching instability, in *Proceedings of the IPAC-2019, Melbourne, Australia*, edited by M. Boland, H. Tanaka, D. Button, and R. Dowd (JACoW, Geneva, Switzerland, 2019), Vol. 10, pp. 3119–3122, 10.18429/JACoW-IPAC2019-WEPTS015.

[12] M. Brosi, Overview of the micro-bunching instability in electron storage rings and evolving diagnostics, in *Proceedings of the International Particle Accelerator Conference IPAC-2021* (JACoW, Geneva, Switzerland, 2021), Vol. 12, pp. 3686–3691, 10.18429/JACoW-IPAC2021-THXA02.

[13] M. Brosi, J. L. Steinmann, E. Blomley, E. Bründermann, M. Caselle, N. Hiller, B. Kehrer, Y.-L. Mathis, M. J. Nasse, L. Rota, M. Schedler, P. Schönfeldt, M. Schuh, M. Schwarz, M. Weber, and A.-S. Müller, Fast mapping of

terahertz bursting thresholds and characteristics at synchrotron light sources, Phys. Rev. Accel. Beams **19**, 110701 (2016).

[14] J. L. Steinmann, T. Boltz, M. Brosi, E. Bründermann, M. Caselle, B. Kehrer, L. Rota, P. Schönfeldt, M. Schuh, M. Siegel, M. Weber, and A.-S. Müller, Continuous bunch-by-bunch spectroscopic investigation of the micro-bunching instability, Phys. Rev. Accel. Beams **21**, 110705 (2018).

[15] A.-S. Müller and M. Schwarz, Accelerator-based THz radiation sources, in *Synchrotron Light Sources and Free-Electron Lasers* (Springer International Publishing, Cham, 2019), pp. 1–35, 10.1007/978-3-319-04507-8_6-2.

[16] M. Klein, K. G. Sonnad, N. Hiller, A. Hofmann, E. Huttel, V. Judin, B. Kehrer, S. Marsching, and A.-S. Mueller, Modeling the low-alpha-mode at ANKA with the accelerator toolbox, in *Proceedings of the 24th Particle Accelerator Conference (PAC-2011), New York* (2011), https://accelconf.web.cern.ch/AccelConf/PAC2011/papers/WEP005.PDF.

[17] A. Papash, E. Blomley, T. Boltz, M. Brosi, E. Bründermann, S. Casalbuoni, J. Gethmann, E. Huttel, B. Kehrer, A. Mochihashi, A.-S. Müller, R. Ruprecht, M. Schuh, J. Steinmann, P. Schreiber, H. T. Boland, D. Button, and R. Dowd, New operation regimes at the storage ring KARA at KIT, in *Proceedings of the IPAC-2019, Melbourne, Australia*, edited by M. Boland, H. Tanaka, D. Button, and R. Dowd (JACoW, Geneva, Switzerland, 2019), Vol. 10, pp. 1422–1425, 10.18429/JACoW-IPAC2019-TUPGW016.

[18] P. Schreiber, T. Boltz, M. Brosi, B. Härer, A. Mochihashi, A.-S. Müller, A. Papash, R. Ruprecht, and M. Schuh, Effect of negative momentum compaction operation on the current-dependent bunch length, in *Proceedings of the International Particle Accelerator Conference No. 12 (IPAC-2021)* (JACoW, Geneva, Switzerland, 2021), pp. 2786–2789, 10.18429/JACoW-IPAC2021-WEPAB083.

[19] P. Schreiber, T. Boltz, M. Brosi, B. Haerer, A. Mochihashi, A. Papash, M. Schuh, and A.-S. Müller, Status of negative momentum compaction operation at KARA, in *CERN Yellow Reports: Conference Proceedings* (CERN, Geneva, 2020), Vol. 9, p. 297, 10.23732/CYRCP-2020-009.297.

[20] H. Wiedemann, *Particle Accelerator Physics* (Springer, Berlin, 2007), Vol. 314.

[21] P. Schönfeldt, A. Borysenko, E. Hertle, N. Hiller, V. Judin, A.-S. Müller, S. Naknaimueang, M. Schuh, M. Schwarz, and J. Steinmann, Fluctuation of bunch length in bursting CSR: Measurement and simulation, in *Proceedings of the 5th International Particle Accelerator Conference (IPAC-2014), Dresden, Germany* (JACoW, Geneva, Switzerland, 2014), pp. 237–239, 10.18429/JACoW-IPAC2014-MOPRO068.

[22] ACST GmbH—Technology solutions for terahertz electronics, https://acst.de/.

[23] M. Caselle, M. Brosi, S. Chilingaryan, T. Dritschler, N. Hiller, V. Judin, A. Kopmann, A. Müller, J. Raasch, L. Rota, L. Petzold, N. Smale, J. Steinmann, M. Vogelgesang, S. Wuensch, M. Siegel, and M. Weber, A picosecond sampling electronic "KAPTURE" for terahertz synchrotron radiation, in *Proceedings of the 3rd International Beam Instrumentation Conference (IBIC-2014), Monterey, CA*, edited by J. Sebek (JACoW, Geneva, Switzerland, 2015), pp. 24–28, https://proceedings.jacow.org/IBIC2014/papers/moczb1.pdf.

[24] M. Brosi, In-depth analysis of the micro-bunching characteristics in single and multi-bunch operation at KARA, Ph.D. thesis, Karlsruhe Institute of Technology, 2020, 10.5445/IR/1000120018.

[25] B. Kehrer, E. Blomley, M. Brosi, E. Bründermann, A.-S. Müller, M. Schuh, P. Schönfeldt, and J. Steinmann, Filling pattern measurements using dead-time corrected single photon counting, in *Proceedings of the 9th International Particle Accelerator Conference IPAC-2018* (JACoW, Geneva, Switzerland, 2018), pp. 2219–2222, https://proceedings.jacow.org/ipac2018/papers/wepal027.pdf.

[26] P. Schönfeldt, P. Schreiber, M. Brosi, J. Schestag, T. Boltz, M. Blaicher, and J. Gethmann, Inovesa/Inovesa: Gamma three, Zenodo, 2019, 10.5281/zenodo.2653504.

[27] P. Schönfeldt, M. Brosi, M. Schwarz, J. L. Steinmann, and A.-S. Müller, Parallelized Vlasov-Fokker-Planck solver for desktop personal computers, Phys. Rev. Accel. Beams **20**, 030704 (2017).

[28] P. Schönfeldt, Simulation and measurement of the dynamics of ultra-short electron bunch profiles for the generation of coherent THz radiation, Ph.D. thesis, Karlsruher Institut für Technologie, 2018, 10.5445/IR/1000084466.

[29] T. Boltz, M. Brosi, E. Bründermann, B. Härer, A.-S. Müller, P. Schreiber, P. Schönfeldt, M. Yan, H. Tanaka Boland, D. Button, and R. Dowd, Perturbation of synchrotron motion in the micro-bunching instability, in *Proceedings of the IPAC-2019, Melbourne, Australia*, edited by M. Boland, H. Tanaka, D. Button, and R. Dowd (JACoW, Geneva, Switzerland, 2019), pp. 108–111, 10.18429/JACoW-IPAC2019-MOPGW018.

[30] T. Agoh, Steady fields of coherent synchrotron radiation in a rectangular pipe, Phys. Rev. ST Accel. Beams **12**, 094402 (2009).

[31] S. Heifets and A. Novokhatski, Coherent beam stability in the low momentum compaction lattice, Phys. Rev. ST Accel. Beams **9**, 044402 (2006).

[32] G. Rakowsky and L. R. Hughey, SURF's up at NBS: A progress report, in *Proceedings of the IEEE Transactions on Nuclear Science* (1979), Vol. 26, p. 3845, 10.1109/TNS.1979.4330628.

[33] U. Arp, G. T. Fraser, A. R. Hight Walker, T. B. Lucatorto, K. K. Lehmann, K. Harkay, N. Sereno, and K.-J. Kim, Spontaneous coherent microwave emission and the saw-tooth instability in a compact storage ring, Phys. Rev. ST Accel. Beams **4**, 054401 (2001).

[34] I. P. S. Martin, C. A. Thomas, and R. Bartolini, Modelling the steady-state CSR emission in low alpha mode at the diamond storage ring, in *Proceedings of the 3rd International Particle Accelerator Conference (IPAC-2012)* (JACoW, Geneva, Switzerland, 2012), pp. 1677–1679, https://accelconf.web.cern.ch/IPAC2012/papers/tuppp031.pdf.

[35] Dimtel Inc., https://www.dimtel.com/.

[36] E. Blomley, Investigation and control of beam instabilities at the Karlsruhe research accelerator using a 3-D digital bunch-by-bunch feedback system, Ph.D. thesis in prepa-

ration, Karlsruhe Institute of Technology, 2021, 10.5445/IR/1000137621.

[37] W. Shields, R. Bartolini, G. Boorman, P. Karataev, A. Lyapin, J. Puntree, and G. Rehm, Microbunch instability observations from a THz detector at Diamond Light Source, J. Phys. Conf. Ser. **357**, 012037 (2012).

[38] G. Wüstefeld, J. Feikes, and M. V. Hartrott, Coherent THz measurements at the metrology light source, in *Proceedings of the IPAC-2010* (2010), p. 3, https://accelconf.web.cern.ch/IPAC10/papers/wepea015.pdf.

[39] K. L. F. Bane, Y. Cai, and G. Stupakov, Threshold studies of the microwave instability in electron storage rings, Phys. Rev. ST Accel. Beams **13**, 104402 (2010).

[40] M. Brosi, J. L. Steinmann, E. Blomley, T. Boltz, E. Bründermann, J. Gethmann, B. Kehrer, Y.-L. Mathis, A. Papash, M. Schedler, P. Schönfeldt, P. Schreiber, M. Schuh, M. Schwarz, A.-S. Müller, M. Caselle, L. Rota, M. Weber, and P. Kuske, Systematic studies of the microbunching instability at very low bunch charges, Phys. Rev. Accel. Beams **22**, 020701 (2019).